



Electronic modulation optimizes OH* intermediate adsorption on Co-Nx-C sites via coupling CoNi alloy in hollow carbon nanopolyhedron toward efficient reversible oxygen electrocatalysis

Yangyang Tan, Zeyi Zhang, Zhao Lei, Liyue Yu, Wei Wu, Zichen Wang, Niancai Cheng*

College of Materials Science and Engineering, Fuzhou University, Fuzhou 350108, China

ARTICLE INFO

Keywords:

CoNi alloy
Hierarchical hollow structure
Bifunctional oxygen electrocatalysts
Electronic regulation
Zn-air batteries

ABSTRACT

Optimizing the electronic structure of the electrocatalyst to adjust the adsorption energies of oxygen intermediates to approach the equilibrium potential ($U_{\text{RHE}}^0 = 1.23 \text{ V}$) is of paramount importance to inhibit the sluggish reaction kinetics of the oxygen reduction/oxygen evolution reaction (ORR/OER), yet remains a huge challenge. Herein, a hierarchical 1D/3D hollow carbon nanopolyhedron with strong electron coupling between the encapsulated CoNi alloy and Co-Nx sites in N-CNTs was designed by a silicon protection-Ni infiltration strategy. Impressively, the optimized CoNi/Co-N@HNC catalyst exhibits high oxygen catalytic activity with a small potential gap of 0.73 V and superior ZABs durability over 350 h. DFT simulation results revealed that coupling with CoNi nanoclusters can effectively downshift the E_d energy levels of the Co adsorption site in CoN₄, dramatically decreased the energy barrier of the rate-determining step (OH* to OH⁻ in ORR; OH* to O* in OER), thereby promote the overall oxygen catalysis reaction kinetics.

1. Introduction

The rechargeable zinc-air battery (ZABs) have shown great energy storage potential due to its environmental friendliness, high theoretical energy density (1084 Wh kg^{-1}) and high safety [1–3]. So far, noble metals platinum carbon (Pt/C) and ruthenium oxide (RuO₂), iridium oxide (IrO₂) still are ORR and OER benchmarks, respectively, but they are not suitable for large-scale application due to their scarcity and inferior bifunctionality [3–5]. Noted that, for the ideal ORR/OER bifunctional catalyst, the Gibbs free energy of each oxygen-containing intermediate should not change ($|\Delta G_{\text{OOH}^*}| = |\Delta G_{\text{O}^*}| = |\Delta G_{\text{OH}^*}| = 0$), indicating no energy waste during the oxygen reaction [6,7]. However, the strong adsorption/desorption force of the oxygen intermediates (*OH, *O, *OOH) cause the sluggish kinetics of oxygen redox reactions, resulting in high overpotentials and enlarged charge/discharge voltage gap, which seriously affects the energy utilization and output power of rechargeable ZABs [8–10]. Therefore, based on the earth-abundant materials, the development of a non-noble metal-based ORR/OER catalyst with a modulated electronic structure to adjust the adsorption energies of oxygen-containing intermediates is of key interest and would be a significant innovation that promotes the large-scale application of ZABs.

Among the noble-metal-free substitutes, M-Nx-C, especially Co-Nx-C, catalysts has exhibited exceptional ORR catalytic performance comparable to commercial Pt/C catalysts, due to the N heteroatom on the carbon substrate optimize the electronic structure of the Co atom at the atomic-level [11–16]. However, its OER activity is still unsatisfactory, resulting in a large ORR and OER potential difference (ΔE), namely high efficiency loss. Theoretically, the adsorption characteristics of oxygen intermediate on the catalytic site depend on the electronic structure of the catalytic site [17]. Recently, some theoretical and experimental studies have demonstrated that the chemical coupling between bimetallic atoms and M-Nx-C can modulate the adsorption energy of oxygen intermediates on M-Nx-C due to the modulated charge distribution of the M-Nx-C sites originated from the electron transfer from metal ions to the nitrogen-doped carbon layer, inducing surprisingly high chemical activities and fast reaction kinetics [18–22]. The constructing a charge-coupled bimetallic alloy/M-Nx-C heterogeneous interface to optimize the charge distribution of M-Nx-C sites has been prove to be an effective strategy to promote reversible oxygen electrocatalysis. For instance, the cooperative interaction between N-doped graphitized CNTs and FeCo nanoparticles (N-GCNT/FeCo) resulted in higher positive charge density on the local surface of pyridine-N-rich GCNTs, which can reduce the energy barrier of the rate determination step (RDS) of

* Corresponding author.

E-mail address: niancaicheng@fzu.edu.cn (N. Cheng).

<https://doi.org/10.1016/j.apcatb.2021.121006>

Received 26 August 2021; Received in revised form 13 November 2021; Accepted 6 December 2021

Available online 10 December 2021

0926-3373/© 2021 Elsevier B.V. All rights reserved.

ORR (OH^* to OH^-) and OER (O^* to OOH^*), and achieve enhanced ORR/OER catalytic activity [23]. Bimetallic FeNi_3 alloy-regulating N-doped carbon ($\text{FeNi}_3@\text{NC}$) can enhance the conversion of OH^- to OH^* in the OER process because the high-efficiency synergistic coupling of FeNi_3 alloy and N-doped carbon makes NC presents an electron-rich state [24]. Although many works have demonstrated the advantages of coupling bimetallic alloys to adjust the electronic structure of M-Nx-C sites, the investigation of adjusting the adsorption energy of oxygen intermediates in specific steps for oxygen redox reactions are still challenging. Furthermore, due to the linear correlation between the adsorption free energies of different oxygen intermediates [6,7,25], efforts to achieve to controllable optimization between oxygen intermediates and superior catalytic performance is always interesting and challenging, and these areas need to be further explored.

According to the DFT calculations by Rossmeisl et al. [25], thermodynamically, the ORR and OER triangle area in the volcano maps on the metal active sites of metal-N-C configuration are subjected to the reduction and generation steps of $^*\text{OH}$ (ΔG_{OH} , $\Delta G_{\text{O}} - \Delta G_{\text{OH}}$), respectively. Motivated by the above considerations, the strong coupling between the encapsulated CoNi alloy and the Co-Nx in the N-CNTs was designed to modulate adsorption energy the OH^* intermediate on M-Nx-C for highly efficient reversible oxygen electrocatalysis. We have constructed a hierarchical 1D/3D hybridization architecture catalyst of size-uniform CoNi alloy nanoparticles encapsulated in self-catalyzed grown Co, N-codoped carbon nanotubes on hollow carbon nanopolyhedron (CoNi/Co-N@HNC) through a silicon protection-Ni infiltration strategy as shown in Scheme 1. This open 1D/3D hierarchical hollow structure catalyst has expanded exposed accessible active sites, rapid electron transfer and mass diffusion, and enhanced structural stability. More importantly, the strong coupling between the encapsulated CoNi alloy and the Co-Nx of N-CNTs can significantly regulate the charge distribution of the latter. Benefit from these advantageous features, the resultant CoNi/Co-N@NC exhibits predominant ORR/OER kinetic activity with a ΔE of 0.73 V. Furthermore, the rechargeable ZABs assembled with CoNi/Co-N@HNC air electrodes showed superior durability over 350 h under current density of 20 mA cm^{-2} , while exhibiting high specific capacity ($816 \text{ mAh g}_{\text{Zn}}^{-1}$) and peak power density (179.1 mW cm^{-2}), significantly superior to the reference $\text{Pt/C}+\text{RuO}_2$ -based ZABs. DFT simulation calculation showed that coupling with CoNi alloy can provide more electrons to transfer to Co-Nx, effectively reduce the E_d energy level of the Co adsorption site in CoN_4 , namely the decrease the adsorption energy of oxygen ($\Delta G_{^*\text{O}} - \Delta G_{^*\text{OH}}$) drive the energy levels of $^*\text{OOH}$ and $^*\text{OH}$ closer to E_b , which dramatically decreased the kinetic energy barrier of the rate-determining step (OH^* to OH^- in ORR; OH^* to O^* in OER), and promotes the reaction kinetic process of ORR/OER in alkaline medium.

2. Experimental section

2.1. Catalysts synthesis

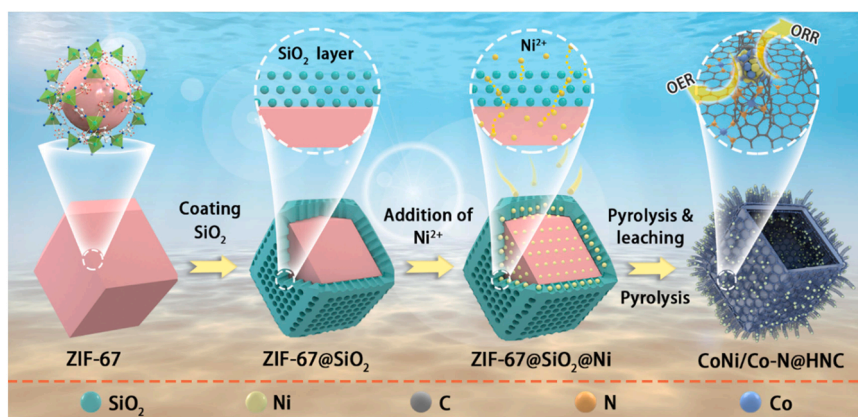
ZIF-67 was prepared according to the literature [26]. After $\text{NH}_3 \cdot \text{H}_2\text{O}$ (0.8 mL) and ZIF-67 were mixed in methanol, TEOS (0.8 mL) was added and stirred for 8 h, then washed and dried (ZIF-67@SiO_2). The obtained ZIF-67@SiO_2 was mixed with 37 mg, 74 mg and 108 mg $\text{Ni(NO}_3)_2 \cdot 6\text{H}_2\text{O}$ (4 wt%, 8 wt%, 12 wt%), respectively, in ethanol solution and stirred and evaporated to dryness at 70°C . The products are denoted as $\text{ZIF-67@SiO}_2@\text{Ni-4}$, $\text{ZIF-67@SiO}_2@\text{Ni-8}$, $\text{ZIF-67@SiO}_2@\text{Ni-12}$, respectively. Subsequently, the dried samples were heat-treated at 700°C in N_2 atmosphere for 2 h, and named as $\text{Co/Co-N@SiO}_2@\text{Ni-4}$, $\text{Co/Co-N@SiO}_2@\text{Ni-8}$, $\text{Co/Co-N@SiO}_2@\text{Ni-12}$, respectively, after natural cooling. The silica shell of the series $\text{Co/Co-N@SiO}_2@\text{Ni}$ (4 wt%, 8 wt%, 12 wt %) were etched by 4 wt% HF acid washing for 12 h, then washed with water until the pH was neutral, and dried overnight at 60°C . Subsequently, the secondary carbonization was carried out at 800°C for 2 h under N_2 atmosphere, and the obtained black powders were named CoNi/Co-N@HNC-4 , CoNi/Co-N@HNC-8 (denoted as CoNi/Co-N@HNC in the manuscript), CoNi/Co-N@HNC-12 catalyst. For comparison, Co/Co-N@NC and CoNi/Co-N@NC samples were synthesized by direct pyrolysis ZIF-67 at 800°C and infiltration of Ni^{2+} (8 wt%) without adding SiO_2 protection and then pyrolysis at 800°C , respectively.

2.2. Materials characterization

Scanning electron microscope (SEM, Supra 55), transmission electron microscope (TEM, Tecnai G2F20) and X-ray powder diffraction (D-MAX 2200 VPC) were used to characterize the morphology and structure of the samples. X-ray photoelectron spectroscopy (XPS) is characterized by K-Alpha. Micromeritics 3Flex equipment was used to determine the N_2 adsorption-desorption isotherm of the sample.

2.3. Electrochemical methods

At room temperature, a three-electrode system on an electrochemical workstation (Autolab) was used for electrochemical testing in a 0.1 M KOH electrolyte saturated with O_2 . The platinum sheet and the Ag/AgCl electrode (saturated KCl) were used as the counter electrode and the reference electrode, respectively, and the working electrode was a glassy carbon electrode (RDE and RRDE) coated with an ink catalyst. The catalyst ink was prepared as follows: 5 mg catalyst powder, 5 wt% Nafion solution (20 μL) and 980 μL mixed deionized water/isopropanol (1:1) solution were mixed uniformly. Then take 10 μL catalyst ink and spread it evenly on the glassy carbon electrode, so that the catalyst loading on the glassy carbon electrode is 0.25 mg cm^{-2} . A loading of 0.1 mg cm^{-2} for commercial Pt/C and RuO_2 were measured as a



Scheme 1. Schematic illustration of the fabrication procedure of the CoNi/Co-N@HNC .

comparison.

2.4. Zinc-air battery assembly

The catalyst ink is prepared as follows: 10 mg catalyst powder, 1.0 mg acetylene black and 5 wt% Nafion solution (30 μL) are added to 1 mL of deionized water/ethanol mixed solution ($= 1:1$) and ultrasonically uniform. The anode is a zinc sheet ($3\text{ cm} \times 6\text{ cm}$), and the air cathode electrode is catalyst ink coated on hydrophobic carbon paper (the effective catalyst area is 0.785 cm^2). For comparison, the loading of Pt/C-RuO₂ (1:1) is $0.2\text{ mg}\cdot\text{cm}^{-2}$. The electrolyte is composed of 0.2 M Zn(CH₃COO)₂ and 6 M KOH. At room temperature, ZABs were tested on the BTS-5V/1–50 mA test system.

3. Results and discussion

3.1. Synthesis and structure characterization

In order to achieve the strong coupling between the encapsulated CoNi alloy and the Co-N_x in the N-CNTs, we construct the hollow structure CoNi/Co-N@HNC electrocatalyst through an improved silicon protection-Ni infiltration strategy of pyrolyzied common ZIF-67, as shown in Scheme 1. Initially, a dodecahedral ZIF-67 coated with a thin mesoporous silica (mSiO₂) shell (ZIF-67@mSiO₂) was achieved. The scanning electron microscopy (SEM) image of SiO₂@ZIF-67 (Fig. S1) showed a relatively rough surface, indicating ZIF-67 was successfully coated by the silicon layer. Thereafter, the designated concentration of Ni²⁺ (8 wt%) passes through the mesoporous silicon layer and enters the

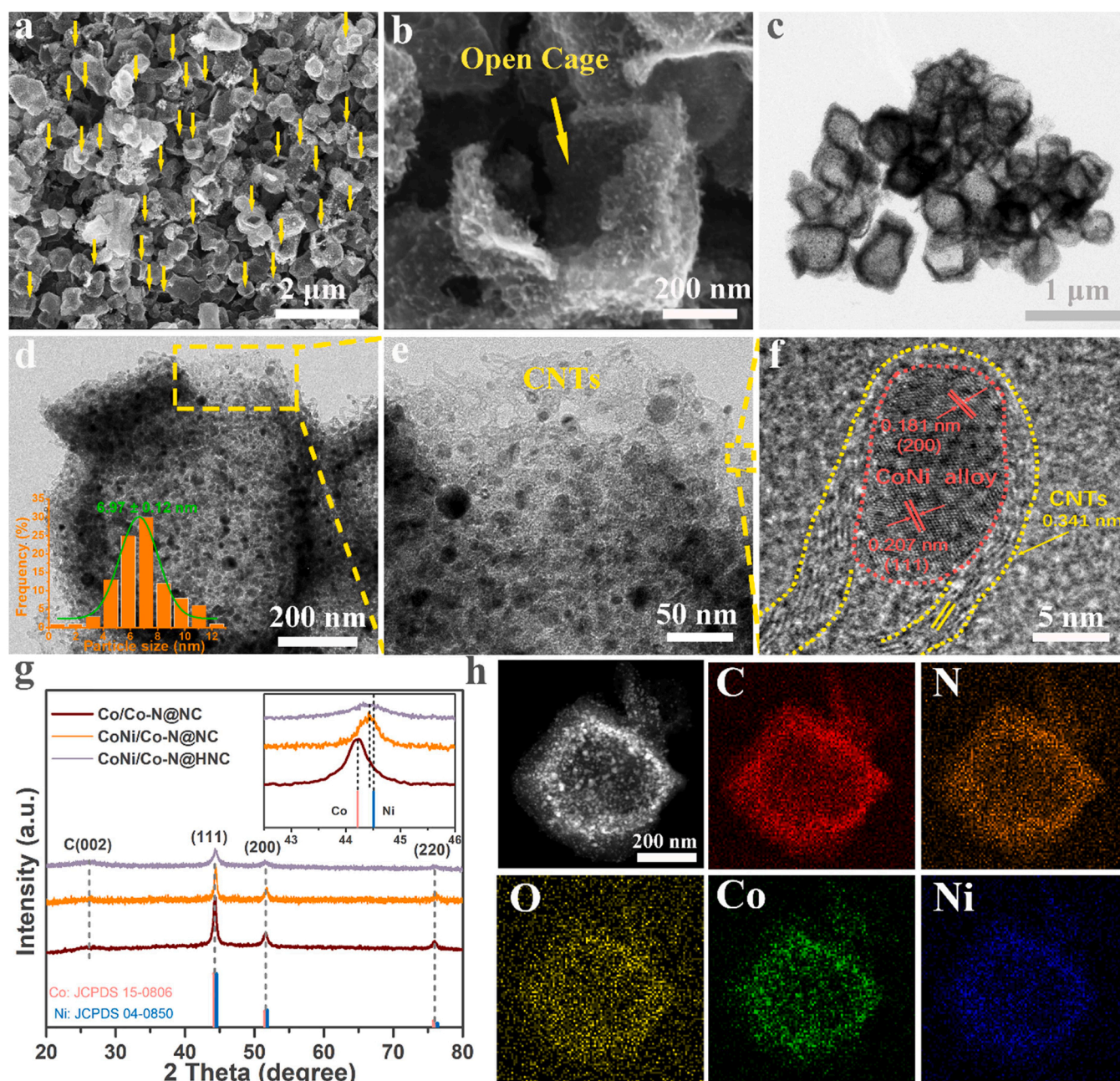


Fig. 1. (a, b) SEM and (c–f) TEM images of CoNi/Co-N@HNC, inset in (d) is the size distribution of CoNi alloy nanoparticles; (g) XRD patterns of Co/Co-N@NC, CoNi/Co-N@NC and CoNi/Co-N@HNC catalyst, the enlarged view of the (111) peak in the inset; (h) HAADF-STEM image and EDX elemental mapping images of CoNi/Co-N@HNC.

pore/cavity of ZIF-67 (Ni@ZIF-67@SiO₂). Subsequently, the obtained Ni@ZIF-67@SiO₂ nanocomposite undergo the first carbonization in N₂ atmosphere at 700 °C, and then CoNi/Co-N@HNC with the open hollow nanopolyhedron structure was obtained by HF acid etching and followed secondary pyrolysis treatment (Fig. 1a, b (yellow arrow), Fig. 1c). The disappearance of the Si signal in the EDX mapping spectrum of CoNi/Co-N@HNC in the Fig. S2 shows that the mSiO₂ layer has been completely removed. The formation of hollow structure is due to carbonation preferentially occurs at the interface between ZIF-67 polyhedron and mSiO₂ layer, making the remaining MOFs in the carbonation process shrink outward to form hollow cavities [27]. Such unique 3D open hollow structure is believed to favor the mass diffusion during the electrocatalysis. Compared with the obvious structural shrinkage and particle aggregation of the pyrolyzed sample without mSiO₂ protection (Fig. S3), the protection of silicon layer preserves the polyhedron morphology of ZIF-67 well, and effectively prevents the irreversible fusion and aggregation of Co and Ni nanoparticles, achieving high density active sites. More importantly, during in secondary carbonization, shell-dwelling Co/Ni NPs catalyze the in-situ growth of CNTs on both inner and outer surfaces of the hollow carbon nanopolyhedron, resulting in the formation of 1D/3D hierarchical structures constructed by CoNi alloy nanoparticle encapsulated carbon-nanotube-grafted hollow carbon shell. The TEM image (Fig. 1d, e) can clearly observe the tangled carbon nanotubes with the embedment of the dark dots growing on the carbon shell. As displayed in the inset of Fig. 1d, these nanoparticles were monodispersed and possessed an average size of 6.97 nm. Notably, the 1D/3D hierarchical structure constructed by the in-situ growth of CNTs on the 3D hollow carbon nanopolyhedron can greatly enhance the charge transfer between the active sites and the matrix and mechanical stability, which is conducive to improving catalytic activity and durability [28,29].

Highly graphitized multi-walled CNTs with an interplanar distance of 0.34 nm can be observed from HRTEM image in Fig. 1f, which corresponds well to the (002) crystal plane of graphite-carbon. In addition, the well-defined 0.181 nm and 0.207 nm lattice fringes of these coated NiCo nanoparticles were observed, which were consistent with the (200) and (111) planes of the of NiCo alloy, respectively. The XRD pattern in Fig. 1g shows that the broad diffraction peak at 26.3° belongs to the graphite carbon (002) plane [30]. The other three diffraction peaks of the obtained sample at 2θ = 44.5°, 51.8° and 76.2° can be indexed to the (111), (200) and (220) faces of face-centered cubic (FCC) CoNi alloys, which is similar to the diffraction patterns of Co (JCPDS 15-0806) and nickel (JCPDS 04-0850), but slightly shifted [31,32]. An enlarged view near the peak (111) in the illustration of Fig. 1g shows that all peak positions are located between pure Ni and pure Co, strongly confirming the formation of a CoNi alloy rather than a single particle of Co and Ni [33]. Furthermore, compared with Co/Co-N@NC and CoNi/Co-N@NC, the characteristic peak of CoNi/Co-N@HNC is broader, indicates that the silicon layer protection strategy can effectively prevent the migration and agglomeration of metal nanoparticles to maintain a smaller size. Raman spectra in Fig. S4 shows that the CoNi/Co-N@HNC has a higher I_D/I_G of 1.16 than Co/Co-N@NC (1.06) and CoNi/Co-N@NC (1.01), indicating it contains more defects, which have been proved to be favorable for ORR/OER [34,35]. Adjusting the concentration of infiltrated Ni²⁺ (4 wt% and 12 wt%), it can be found that all three samples show a hollow structure (Figs. S5 and S6), and CoNi/Co-N@HNC (8 wt%) has a more excellent 1D/3D structure containing more densen carbon nanotubes, that is expected to have better catalytic performance. In addition, the XRD spectrum in Fig. S7 indicates that the size of CoNi alloy nanoparticles gradually increased with the increase of the amount of Ni²⁺. Not only that, the secondary carbonization at 800 °C is critical for the formation of CoNi alloys, which can repair the carbon structure and improve the catalytic conductivity (Fig. S8). The dark field STEM and corresponding EDX elemental mapping (Fig. 1h) also clearly reveals that the uniform distribution of C, N, O elements in the whole hollow carbon skeleton structure, while Ni and Co

are concentrated distributed in the nanoparticle region, which further proves the formation of CoNi alloy NPs.

The influence of the protection strategy of the silicon layer on the pore structure of the obtained different samples were analyzed by measuring the N₂ adsorption/desorption isotherm and the pore size distribution (Fig. 2a). The adsorption/desorption isotherms of the Co/Co-N@NC, CoNi/Co-N@NC and CoNi/Co-N@HNC samples all show the obvious hysteresis loops in the medium pressure range (P/P₀ = 0.4–0.95) (Type IV isotherm), indicating the coexistence of micropores and mesopores in the samples [36]. However, the specific surface area and cumulative pore volume of CoNi/Co-N@HNC were 352 m²g^{−1} and 0.388 m³g^{−1}, respectively, much higher than the corresponding values of Co/Co-N@NC (216 m²g^{−1} and 0.281 m³g^{−1}) and CoNi/Co-N@NC (173 m²g^{−1} and 0.143 m³g^{−1}) (Table S1). Obviously, the direct infiltration of Ni²⁺ without the protection of silicon layer reduces the specific surface area and pore volume of ZIF-67 derivatives, while the CoNi/Co-N@HNC obtained by the protection of silicon layer exposes more micro-mesoporous.

and higher pore volume due to the hollow structure. This conclusion is further supported by the formation of pores at about 0.5 nm and the high porosity of different micropore sizes of CoNi/Co-N@HNC in the illustration of Fig. 2a. Structurally, CoNi/Co-N@HNC catalyst with the hierarchical microporous-mesoporous-macroporous interconnection 1D/3D hollow structure can effectively accelerate the mass diffusion and charge transfer in the oxygen catalysis process, and thus hopefully enhance the accessibility of active sites.

In order to reveal the effect of infiltration Ni²⁺ on the surface elements of the CoNi/Co-N@HNC catalyst, we further analyzed its chemical and electronic states by X-ray photoelectron spectroscopy (XPS) measurements. The XPS survey spectrum in Fig. S9 reveals that the CoNi/Co-N@HNC is consisted of C, N, O, Co and Ni elements. The N 1s spectrum (Fig. 2b) reveal five main species including pyridinic N (397.8 eV), Co-Nx (398.8 eV), pyrrolic N (399.9 eV), graphitic N (401.6 eV) and oxidized N (402.8 eV) [37,38]. Clear negative shift in the binding energy of the N 1s peaks of CoNi/Co-N@HNC compared to those of Co/Co-N@NC are observed, which may be caused by the migration of partial electron of CoNi alloy to the N atom, thus optimizing the surface electronic structure of CoNi/Co-N@HNC [21]. Fig. 2c, Tables S2 and S3 show the detailed N content of the as-prepared samples. The higher Co-Nx and graphitic-type nitrogen content in CoNi/Co-N@HNC than that in Co/Co-N@NC indicate that the formation of CoNi alloy enhances the interaction with the carbon layer, and catalyzes the generation of graphitized carbon nanotubes, thus improving the electrical conductivity of the catalyst [39–41]. Meanwhile, the high-resolution Co 2p spectra of CoNi/Co-N@HNC in Fig. 2d could be clearly divided into three doublets corresponding to the metallic Co species (778.5 / 793.7 eV), the N-coordinated Co component (Co-Nx) (780.1 / 796.3 eV) and associated the satellite peaks at 783.3 and 802.7 eV [11,42], indicating the coexistence of CoNi alloy NPs and Co-Nx in CoNi/Co-N@HNC. Similarly, the high resolution Ni 2p spectra (Fig. 2e) of CoNi/Co-N@HNC have two peaks centered at 851.8 eV and 869.5 eV corresponding to metallic Ni phase, and the two peaks at 855.8 eV and 873.6 eV, assignable to the Ni²⁺ 2p_{3/2} and Ni²⁺ 2p_{1/2}, respectively [32, 43]. In the Ni 2p spectrum, the peak of the Ni²⁺ ionic state is much larger than the peak of the zero-valent metal, which may be due to the high sensitivity of the small CoNi NPs to air and surface oxidation, which is consistent with the CoNi alloy-encapsulated carbon materials reported previously [32,44]. Compared with Co/Co-N@NC (8.2 at%), the content of zero-valent Co metal in the Co 2p spectra of CoNi/Co-N@HNC (30.5 at%) (Table S4) is obviously increased, indicating the introduction of Ni makes Co and Ni mainly exist in the form of CoNi alloy in the CoNi/Co-N@HNC. Not only that, compared with Co/Co-N@NC, the Co-Nx peak of CoNi/Co-N@HNC moved to the side of the lower binding energy, while the position of the Co⁰ peak remains unchanged. This indicates that the introduction of Ni components triggered the interaction between the CoNi alloy and the Co-Nx species, which may lead to

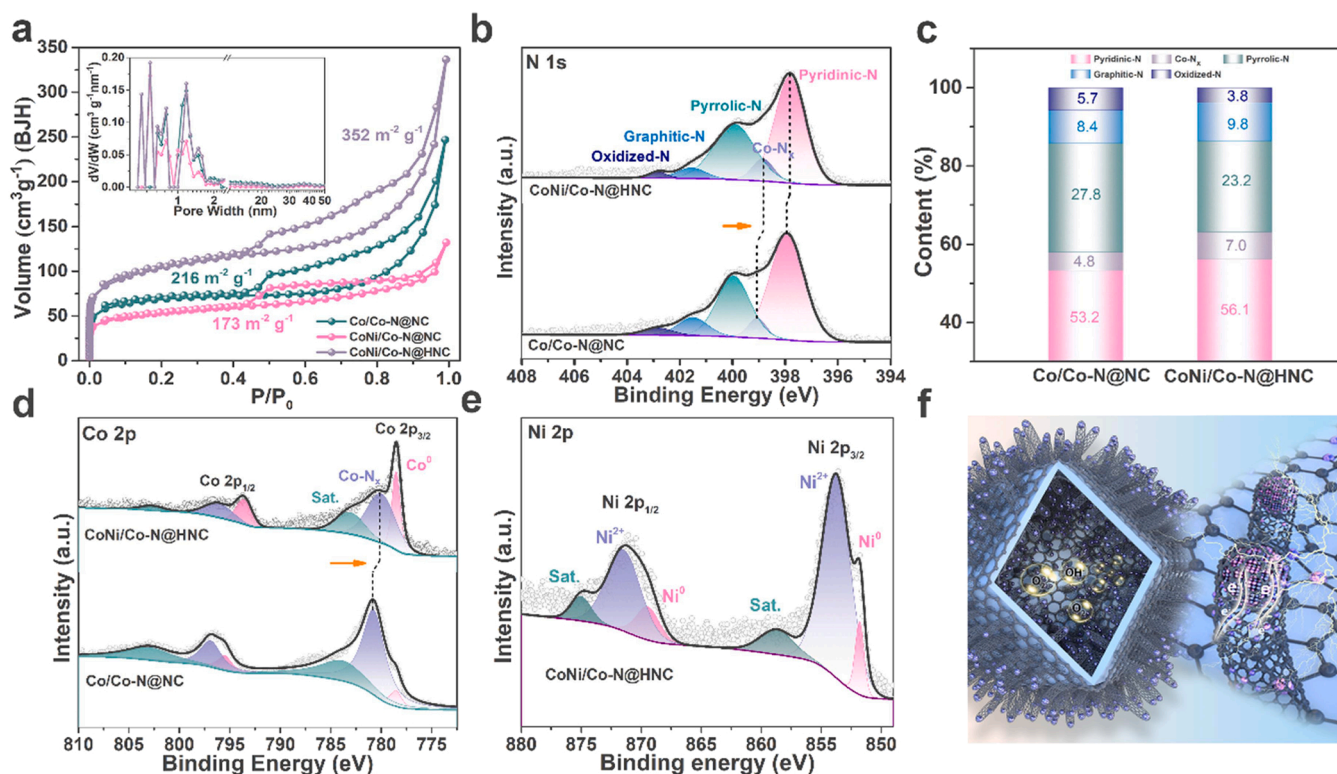


Fig. 2. (a) N₂ adsorption-desorption isotherm of Co/Co-N@NC and CoNi/Co-N@HNC catalyst (pore size distribution exhibited in inset); (b) HR-XPS spectra of N 1s and (c) Co 2p for Co/Co-N@NC and CoNi/Co-N@HNC catalyst; (d) HR-XPS spectra of Ni 2p for CoNi/Co-N@HNC. (f) Schematic diagram of the structure and electronic effects of CoNi/Co-N@HNC in O₂-to-OH⁻ conversion.

the more electrons transfer from Ni to Co-N_x, thereby endows the Co atom in the Co-N_x species a higher electron density, which corresponds to the negative shift of the Co-N_x peak in Fig. 2b. Furthermore, as shown in Fig. S10, as the amount of Ni²⁺ infiltration increases, the Co⁰ and Ni⁰ peaks of the series of CoNi/Co-N@HNC samples gradually increase, while the N1s peak gradually shifts negatively, indicating that the increase in the CoNi alloy content further enhanced the electronic coupling with Co-N_x in N-CNTs. These results further confirm the successful combination of the CoNi alloy and the N-doped carbon nanotubes, thereby form a closely-connecting CoNi/Co-N_x active site distribution structure. The strong electronic coupling between them can effectively regulate the charge distribution of the active sites of Co-N, thus promoting the electrocatalytic process. Therefore, the CoNi/Co-N@HNC catalyst with 1D/3D structure design and active site charge regulation (Fig. 2f) is expected to achieve fast reaction kinetics and high conversion efficiency in oxygen catalysis.

3.2. ORR and OER catalytic activity

The ORR/OER electrocatalytic activity of the synthesized CoNi/Co-N@HNC was evaluated in alkaline medium. As shown in Fig. 3a, CoNi/Co-N@HNC exhibits a higher onset potential of 0.96 V (vs RHE, the same below) and a more positive half-wave potential of 0.86 V (vs RHE) than Co/Co-N@NC (0.92 and 0.83 V, respectively), CoNi/Co-N@NC (0.93 and 0.84 V, respectively) and exceeds the currently reported Co-based electrocatalyst (Table S5), and comparable to the benchmark Pt/C catalyst (1.00 and 0.85 V, respectively), evincing its high catalytic activity. The tafel slope for CoNi/Co-N@HNC is 36.9 mV dec⁻¹ (Fig. 3b), lower than commercial Pt/C catalyst (59.1 mV dec⁻¹) and other as-prepared catalysts, suggesting fast ORR reaction kinetics. The ORR mechanism of CoNi/Co-N@HNC was further investigated by the rotating disks testing in Fig. S11a,b, suggesting an effective 4e⁻ reduction pathway [45,46]. In addition, the RRDE test (Fig. S11c)

showed that CoNi/Co-N@HNC catalyst exhibited higher n values (3.83–3.92) and lower HO₂⁻ yields with approximately 2.3–7.8% in a range of 0.2–0.8 V than Co/Co-N@NC and CoNi/Co-N@NC, which further confirms the highly selective four-electron paths. Apart from the high activity, the half wave potential of CoNi/Co-N@HNC showed no obvious shift after 5000 cycles ($\Delta E \approx 8$ mV), which obviously outperforms that of Pt/C ($\Delta E \approx 56$ mV) (Fig. 3c), indicating the high structural stability and catalytic durability of CoNi/Co-N@HNC. In addition, the i-t curve of CoNi/Co-N@HNC did not change significantly when introduced methanol into O₂-saturated electrolyte (Fig. S11d), while Pt/C decreased sharply, reflecting its good methanol cross-over tolerance during ORR. Simultaneously, the OER activity of CoNi/Co-N@HNC was further evaluated under the same test conditions. As shown in Fig. 3d, CoNi/Co-N@HNC show a potential ($E_{j=10}$) of 1.58 V under a metric current density of 10 mA·cm⁻², much smaller than Co/Co-N@NC (1.66 V), CoNi/Co-N@NC (1.68 V) and the RuO₂ material (1.64 V), as well as the well-developed transition metal alloy catalysts reported recently (Table S6). The CoNi/Co-N@HNC possesses the smallest tafel slope of 105.8 mV dec⁻¹ among all samples (Fig. 3e), suggesting a superior OER kinetics[47]. Inadequate active sites (Co/Co-N_x) and inefficient electronic regulation of Co/Co-N@NC as well as structural collapse and CoNi NPs agglomeration of CoNi/Co-N@NC are the main reasons for their low catalytic activity. The long-term durability test showed that the performance of CoNi/Co-N@HNC did not decay significantly after continuous operation of 10 h at 10 mA·cm⁻², while the benchmark RuO₂ increase 173 mV after 9 h test, suggesting the as prepared CoNi/Co-N@HNC has high OER catalytic stability (Fig. 3f). The excellent ORR/OER catalytic stability and activity of CoNi/Co-N@HNC catalyst further proves the superiority of the silicon layer protection and subsequent Ni infiltration strategy in this work, that is, under the premise of preventing metal particle agglomeration, the in-situ constructed 1D/3D hierarchical hollow structure and the introduction of Ni²⁺ to form CoNi/Co-N_x active

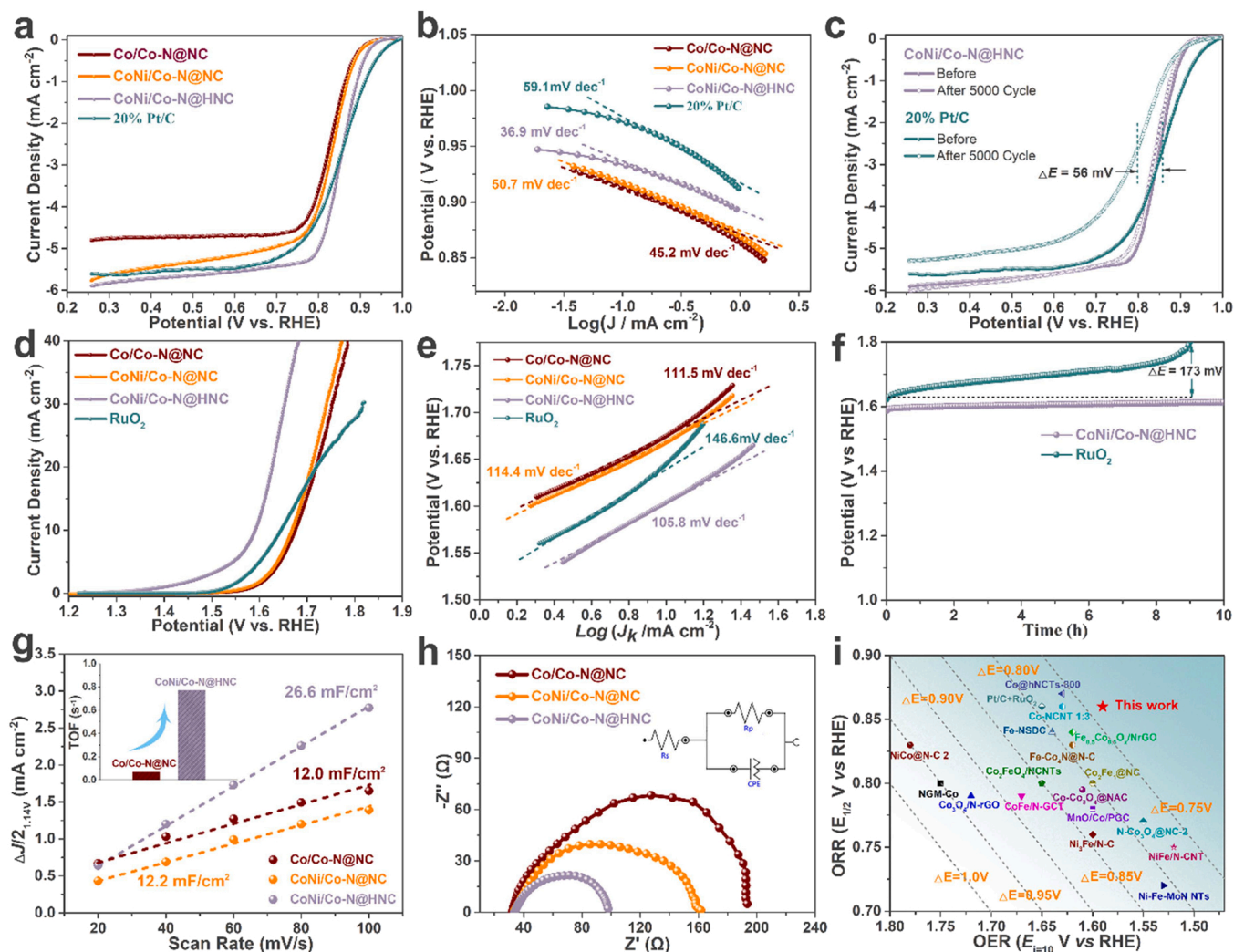


Fig. 3. (a) ORR curves and (b) Corresponding Tafel plots of various catalysts in O₂-saturated 0.1 M KOH solution at 1600 rpm (scan rate: 10 mV s⁻¹), (c) ORR LSV curves of the CoNi/Co-N@HNC and 20% Pt/C catalyst before and after 5000 cycles for the. (d) OER curves, (e) Tafel plots and (f) OER durability at 10 mA cm⁻² of various catalysts. (g) Electrochemical active surface areas of various catalysts, the inset in (g) shows corresponding TOF values (measured at 1.6 V vs RHE) calculated based on all metal sites of Co/Co-N@NC and CoNi/Co-N@HNC; (h) EIS Nyquist plots of various catalysts, the inset is the fitting circuit. (i) OER and ORR activities of CoNi/Co-N@HNC in 0.1 M KOH compared with Pt/C+RuO₂ and representative transition metal-based catalysts. The dotted lines refer to ΔE at the same values.

site, thus modulates the electronic structure of Co-N_x site.

The electrochemical double-layer capacitance (Cdl) and electrochemical active surface area (ECSA) derived from the cyclic voltammetry (CV) curve in the non-Faraday range were performed to further evaluate the advantages of CoNi/Co-N@HNC in catalyst/electrolyte interfaces for catalytic sites and rapid reactant migration (Figs. S12 and 3g) [48,49]. As shown in Fig. 3g, the Cdl value (26.6 mF cm⁻²) of CoNi/Co-N@HNC was more than twice that of Co/Co-N@NC (12.0 mF cm⁻²) and CoNi/Co-N@NC (12.2 mF cm⁻²), indicating its higher ECSA, namely the combination of CoNi/Co-N_x active sites and 1D/3D hollow structure carbon substrate is favorable to exposure more accessible active sites, which is consistent with its higher specific surface area. Moreover, compared with Co/Co-N@NC (0.067 s⁻¹), the sharply increased TOF values (0.773 s⁻¹) of CoNi/Co-N@HNC in the illustration further verified that the introduction of Ni and the formation of hollow structure greatly promote the oxygen catalytic activity of CoNi/Co-N@HNC. This was further supported by the electrochemical impedance spectroscopy (EIS) measurements. From the Nyquist plot (Fig. 3h), CoNi/Co-N@HNC has a significantly smaller semicircle in the intermediate frequency region in the three samples, indicating its lowest charge transfer resistance (Table S7) [50]. These results indicate that the hollow structure of CoNi/Co-N@HNC facilitates the expose more active

sites for the oxygen catalytic reaction and improve its electron transfer kinetics, contributing to the improvement of ORR/OER electrocatalytic performance. The excellent bifunctional properties of CoNi/Co-N@HNC oxygen electrocatalysts was further confirmed by ΔE evaluation. As shown in Fig. S13, CoNi/Co-N@HNC catalyst has the lowest ΔE (0.73 V) among the as-prepared catalysts and the noble metal catalyst (RuO₂-Pt/C), further verified the superiority of hierarchically 1D/3D structure and strong synergy between CoNi alloy and Co-N_x sites in in-situ grown nitrogen doped carbon nanotubes. Moreover, a comparison of ORR/OER catalytic activity (Fig. 3i) with that of recently reported transition metal and heteroatom-doped carbon composite catalyst further demonstrates the excellent bifunctional oxygen catalytic performance of CoNi/Co-N@HNC in our work. In addition, CoNi/Co-N@HNC obtained at a Ni²⁺ concentration of 8 wt% exhibits the best ORR/OER catalytic activity (Fig. S14), indicating that although CoNi/Co-N@HNC-12 has a stronger charge coupling of CoNi/Co-N_x (Fig. S10), the more well-defined 1D/3D hierarchical hollow structure of CoNi/Co-N@HNC also plays a key role in promoting the catalytic activity of oxygen than other Ni²⁺ concentrations. Furthermore, as shown in Fig. S15, the ORR/OER performance of the obtained catalyst is observed to be positively correlated with its N content, especially the Co-N_x content, indicating the higher N and Co-N_x content in

CoNi/Co-N@HNC can improve the ORR/OER performance. In order to further reveal the main contribution of Co-N-C sites as ORR/OER, we used similar methods to replace ZIF-67 and Ni^{2+} with ZIF-8 and Co^{2+} , respectively, to obtain Co/Co-N@HNC, and then removal Co through acid etching to obtain the hollow structure Co-N-C catalyst Co-N@HNC. The XRD and TEM in Fig. S16 prove that a small amount of Co particles are still present. According to XPS analysis (Fig. S16c), the Co^0 content of Co-N@HNC is only 4.7 wt%, while the Co-N content is 75.1 wt%, which indicates that Co-N is the main form of Co in Co-N@HNC. As shown in Fig. S16d,e, compared with CoNi/Co-N@HNC, the ORR and OER performance of Co-N@HNC did not significantly decrease, indicating that Co-N-C is the main active site for ORR and OER. Based on the above analysis, the distinguished ORR/OER activity of CoNi/Co-N@HNC is attributed to the following: 1) In situ grown carbon nanotubes increase the contact area between the local catalyst surface and O_2/OH^- , while hollow structures expose more active sites [37]; 2) The strong coupling effect between CoNi alloy and Co-Nx sites in N-doped carbon nanotubes can regulate the inherent electronic structure of Co-Nx sites and promote oxygen-related adsorption/desorption processes [51]; 3) The 1D/3D hybrid conductive structure formed by N-doped carbon nanotubes and hollow carbon nanopolyhedron can improve the transport of electrons and oxygen molecules and promote the kinetics of oxygen catalytic interface reaction.

3.3. Catalytic mechanism and DFT calculations

DFT calculations were executed to further elucidate the crucial role of CoNi alloy in activating surface Co-Nx adsorption sites and the internal synergistic mechanism between surface electronic structure of Co-Nx sites and ORR/OER catalytic intermediates. Three models of bare

Co-N₄-CNTs, Co/Co-N₄-CNTs and CoNi/Co-N₄-CNTs were constructed by a Co-N₄ site doped (6,6) single-walled carbon nanotubes, a Co₅ nanocluster and a Co₂Ni₃ nanocluster encapsulated in Co-N₄ site doped (6,6) single-walled carbon nanotubes, respectively, which have been validated as effective geometric models to explore the basic electronic structure of carbon nanotube-encapsulated metal systems [23, 52]. Based on the references of Nørskov et al. [7,8], both ORR and OER

involve four elementary steps, in which ORR generates through the formation of OOH^* from adsorbed O_2 , and then further reduces to O^* and OH^* (* represents the active site), while the OER happened in the opposite direction (Fig. 4a). According to the differential charge diagram in Figs. 4c and S17, compared with Co-N₄-CNTs, the construction of Co nanocluster/Co-N₄-CNTs interface caused partial electrons transfer from the metal Co cluster to Co-N₄ site, resulting in the non-uniform charge distribution at local Co-N₄ sites in N-CNTs. Furthermore, the introduction of Ni atoms accelerated the transfer of charge from the Ni cluster to the Co-N₄ site (Fig. S18), which further regulated the electronic structure of the Co-N₄ sites in CoNi/Co-N₄-CNTs. The calculated projected density of states (PDOS) in Fig. 4b also showed that CoNi/Co-N₄-CNTs has the highest density of electron states near the Fermi level among the three models, indicating that the introduction of Ni could further improve the electronic conductivity of CoNi/Co-N₄-CNTs catalysts, ensuring faster electron transfer during ORR/OER process [53]. The corresponding d-band centers (E_d) energy levels in Fig. 4c shows that the d-band center (−0.84 eV) of Co in the CoNi/Co-N₄-CNTs was lower than that of Co-N₄-CNTs (−0.73 eV) and Co/Co-N₄-CNTs (−0.82 eV), which was due to the orbital hybridization of Ni atom with Co atom and N atom, leads to the d orbital of Co in CoNi/Co-N₄-CNTs gained more electrons. Since the energy level of the d-band center determines the degree of electron filling of the antibonding state, it determines the stability and strength of the adsorption bond [17,54]. The longer Co-O bond length of the oxygen-containing intermediate on the surface Co site in CoNi/Co-N₄-CNTs than Co-N₄-CNTs and Co/Co-N₄-CNTs verifies this (Fig. S19), which was favorable for the desorption behavior and subsequent reactions of intermediate on CoNi/Co-N₄-CNTs, thus accelerating the ORR/OER reaction process. In order to further explore the effect of Ni atoms on the catalytic activity of CoNi/Co-N₄-CNTs, we calculated the free-energy profile of ORR/OER at $U = 1.23$ V on the surface Co sites of the three models (Fig. 4d). For ORR catalytic, the rate-determining step (RDS) is the desorption of OH^* (OH^* to OH^-), but the high RDS energy barriers of Co-N₄-CNTs ($|\Delta G_{\text{OH}^*}| = 0.72$ eV) and Co/Co-N₄-CNTs ($|\Delta G_{\text{OH}^*}| = 0.67$ eV) are not conducive to the reversible OER catalytic reaction and hinder the reaction kinetics process. In contrast, when Ni is introduced into the Co cluster/N-CNTs

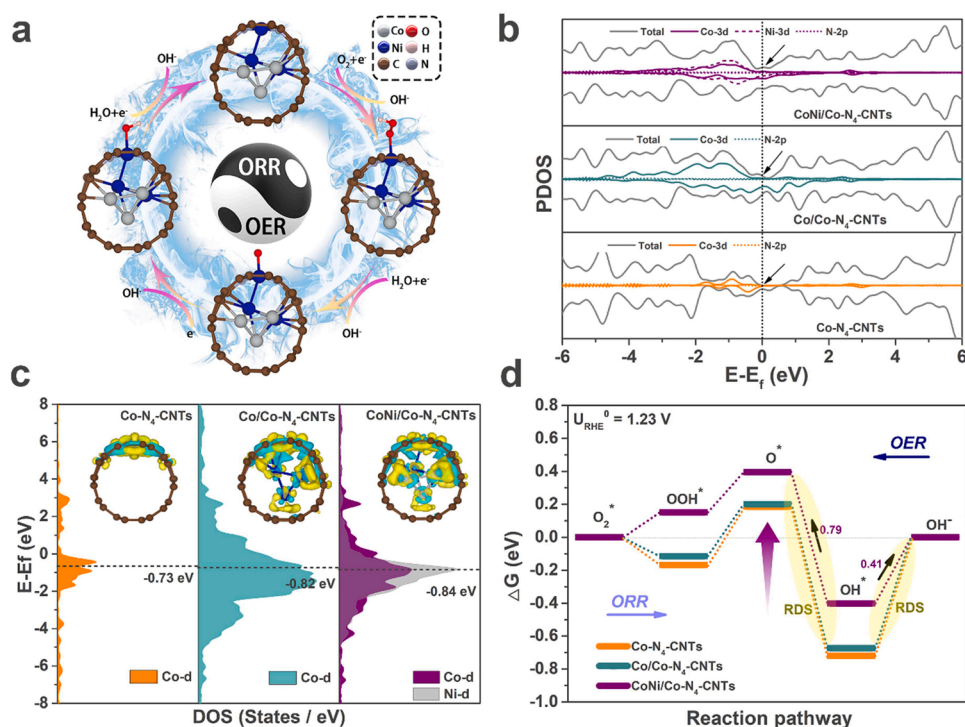


Fig. 4. (a) Schematic diagram of ORR kinetic process occurring on the surface of catalytic model in alkaline medium. (b) The projected density of states (PDOS) on Co-N₄-CNTs, Co/Co-N₄-CNTs, CoNi/Co-N₄-CNTs model. (c) Density of states (DOS), D-band centers and corresponding the charge density redistributions of Co-N₄-CNTs, Co/Co-N₄-CNTs, CoNi/Co-N₄-CNTs model (side view, the blue and yellow isosurfaces show the electron losing and gaining, respectively); (d) The free energy diagrams of ORR and OER at the equilibrium potential on various catalysts model.

interface, the RDS energy barrier of CoNi/Co-N₄-CNTs is reduced to 0.41 eV; As for OER, CoNi/Co-N₄-CNTs also has the lowest RDS (OH* to O*) energy barrier of 0.79 eV, lower than Co-N₄-CNTs (0.90 eV) and Co/Co-N₄-CNTs (0.87 eV), which were consistent with the experimental results. Overall, the reaction barriers of the three important intermediates (OOH*, O*, OH*) of CoNi/Co-N₄-CNTs are all significantly optimized after the introduction of Ni, namely the decrease the adsorption energy of oxygen ($\Delta G_{O^*} - \Delta G_{OH^*}$) drives the energy levels of OOH* and OH* closer to the E_f ($|\Delta G_{OOH^*}| \approx |\Delta G_{O^*}| \approx |\Delta G_{OH^*}| \rightarrow 0$), thereby optimizing the entire ORR/OER process. In addition, the ORR and OER limiting potentials calculated by Gibbs free energy changes at different electrode potentials in Fig. S20 also show that CoNi/Co-N₄-CNTs has the lowest ORR and OER limiting potential among all model. Therefore, the theoretical and experimental results are in an excellent accordance, indicating that coupling with CoNi nanoclusters can effectively optimize the electronic structure of CoN₄ sites in N-CNTs, thereby reducing the energy barrier of reaction intermediates, especially OH* in RDS, and promoting the reversible ORR/OER kinetics process.

3.4. Rechargeable Zn-air battery test

Encouraged by the superior ORR/OER properties of CoNi/Co-N@HNC, we evaluated its application as an air cathode catalyst in practical ZABs (Fig. 5a). Fig. 5b shows that the open circuit potential (OCP) of ZAB based on CoNi/Co-N@HNC is 1.47 V, superior to Pt/C-RuO₂ catalyst (1.43 V), and the recently reported bifunctional catalysts (Table S8). Due to its excellent reversible oxygen catalytic activity, CoNi/Co-N@HNC exhibits a narrower voltage gap than Pt/C+RuO₂ in the charge and discharge polarization curve of Fig. 5c. The peak power density of CoNi/Co-N@HNC-based ZABs is 179.1 mW·cm⁻² (Fig. 5d), higher than Pt/C-RuO₂ (91.8 mW·cm⁻²) and many recent Co-based ZABs (Table S8). At a discharge current density of 10 mA cm⁻² based on the mass loss of Zn, CoNi/Co-N@HNC exhibited an impressive specific capacity of 816 mAh·g_{Zn}⁻¹ (Fig. 5e), corresponding to an energy density of 1020 Wh kg_{Zn}⁻¹, exceeding the benchmark Pt/C-RuO₂ (762 mAh·g_{Zn}⁻¹; 914 Wh·kg_{Zn}⁻¹) and many reported state-of-art ZABs (Table S8). Moreover, under different discharge current densities, CoNi/Co-N@HNC also exhibited considerable rate capability in Fig. 5f. The long-term cyclability test under 20 mA·cm⁻² shows that CoNi/Co-N@HNC has a narrow initial voltage gap of 1.15 V, and there is no

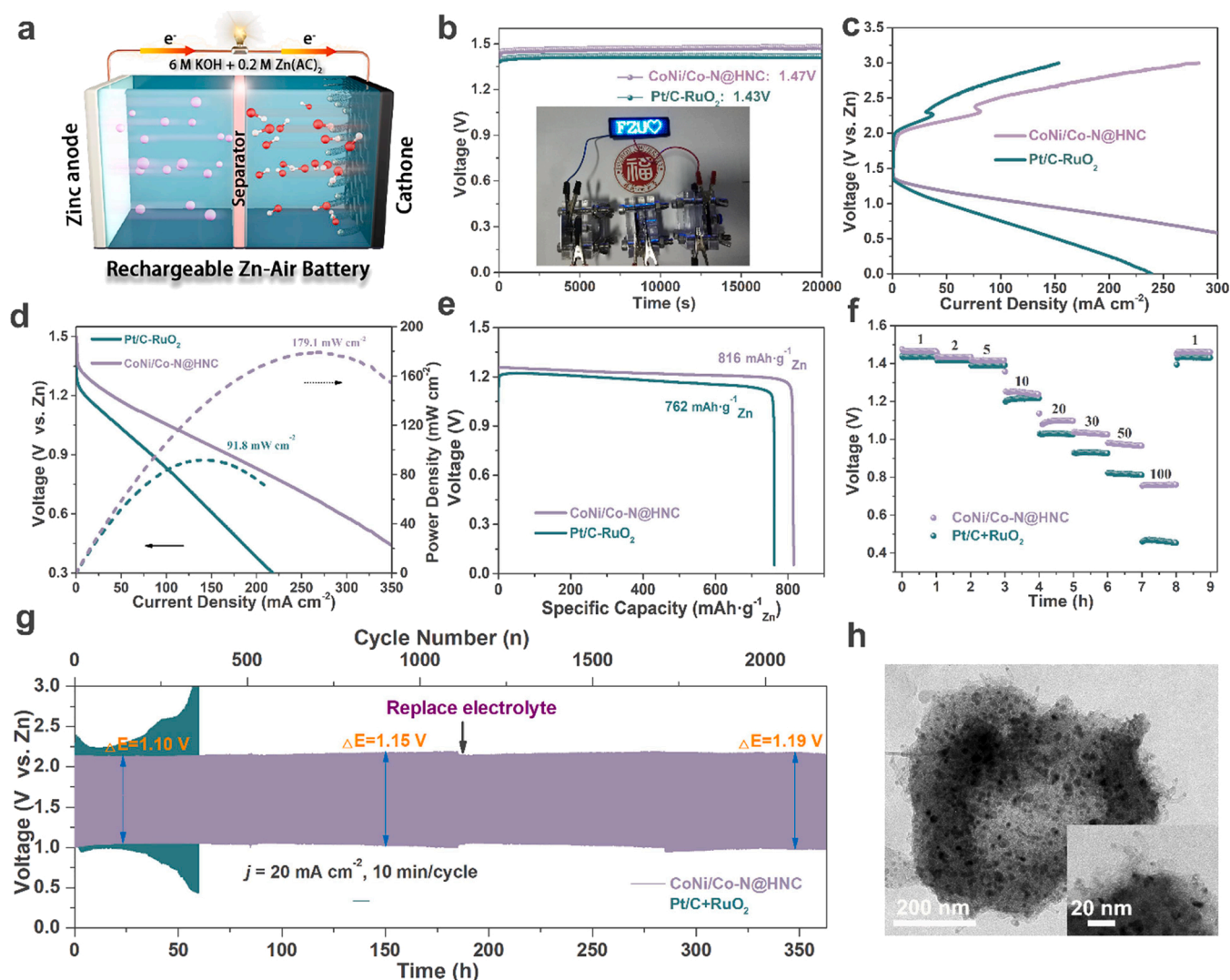


Fig. 5. Performance of rechargeable ZABs. (a) Schematic configuration of the homemade ZABs. (b) OCP plot of CoNi/Co-N@HNC and Pt/C-RuO₂, the illustration is optical image of a LED panel lighted by three ZAB in series. (c) Charge and discharge polarization (V-j) curves, and (d) the corresponding power density curves, (e) Specific capacities plots at 10 mA·cm⁻², (f) Discharge curves at various discharge current densities of CoNi/Co-N@HNC and Pt/C-RuO₂. (g) Galvanostatic discharge cycling curves at 20 mA·cm⁻² of rechargeable CoNi/Co-N@HNC and Pt/C-RuO₂ based Zn-air batteries. (h) TEM image of CoNi/Co-N@HNC after cycling.

significant voltage attenuation after cycling for more than 350 h (more than 2000 cycles), which is far better than the cycle time of Pt/C+RuO₂-based ZABs (only 50 h) (Fig. 5g). By connecting three CoNi/Co-N@HNC-based ZABs in series (the illustration Fig. 5b) to power a commercial LED (3.8 V), indicating its outstanding activities and application prospects in electronic products. In addition, as shown in Figs. 5h and S21, the TEM image taken after 350 h cycle clearly shows that the well-protected carbon nanotubes wrapped with CoNi nanoparticles are still stably fixed on the hollow carbon matrix without obvious aggregation and morphological changes. In addition, the XPS of the post-catalyst CoNi/Co-N@HNC after a long charge-discharge cycle (Fig. S19e and f) shows that although a new peak attributed to the CoOOH phase was observed at 779.74 eV in the Co2p of the post-catalyst [55–60], the main phases of Co and Ni did not transformation significantly due to the protective effect of the graphite carbon layer on the CoNi alloy, demonstrating excellent catalysis and structural stability.

4. Conclusions

In summary, in order to achieve controllable regulation of oxygen-containing intermediates during oxygen catalysis, we have carefully designed a hierarchical 1D/3D hollow carbon nanopolyhedron electrocatalyst (CoNi/Co-N@HNC) with strong electron coupling between the encapsulated CoNi alloy and Co-Nx sites in N-CNTs by a silicon protection-Ni infiltration strategy. Benefiting from the open hollow carbon substrate, the closely-combined hierarchical 1D/3D structure and the strong charge regulation of Co-Nx sites by the CoNi alloy, the optimized CoNi/Co-N@NC catalyst exhibits excellent reversible oxygen catalytic activity and stability. The ORR/OER potential gap of CoNi/Co-N@HNC is only 0.73 V, and as the air cathode used for ZABs in practical applications can be circulated for more than 350 h, and present a high power and specific capacity of 179.1 mW·cm⁻² and 816 mAh·g_{Zn}⁻¹, which are far better than the Pt/C-RuO₂ catalyst. DFT calculations reveal that coupling with CoNi nanoclusters can effectively reduce the d-band center of the Co adsorption site in CoN₄, thereby optimizing the desorption capacity of oxygen-containing intermediates on Co sites, and significantly decreased the kinetic energy barrier of the rate-determining step (OH* to OH⁻ in ORR; OH* to O* in OER), thus accelerating the overall ORR/OER reaction kinetics process. This work provides a reference to regulate and optimize oxygen intermediates on transition metal-based oxygen electrocatalysts toward high-performance ZABs.

CRediT authorship contribution statement

Yangyang Tan: Investigation, Validation, Data curation, Visualization, Writing – original draft. **Zeyi Zhang:** Software, Formal analysis. **Zhao Lei:** Data Curation. **Liyue Yu:** Visualization. **Wei Wu:** Investigation. **Zichen Wang:** Formal analysis. **Niancai Cheng:** Conceptualization, Writing – review & editing, Supervision, Project administration.

Declaration of Competing Interest

The authors declare that they have no known competing financial interests or personal relationships that could have appeared to influence the work reported in this paper.

Acknowledgments

The authors acknowledge support from the National Natural Science Foundation of China (Grant No. 21875039), Minjiang Professorship (XRC-1677), Fujian Province's High Level Innovative and Entrepreneurial Talents (50012709), the Open Project Program of the State Key Laboratory of Photocatalysis on Energy and Environment (Grant No. SKLPEE-201814), Fuzhou University.

Appendix A. Supporting information

Supplementary data associated with this article can be found in the online version at doi:10.1016/j.apcatb.2021.121006.

References

- [1] Y. Li, H. Dai, Recent advances in zinc-air batteries, *Chem. Soc. Rev.* 43 (2014) 5257–5275, <https://doi.org/10.1039/c4cs00015c>.
- [2] H.-F. Wang, Q. Xu, Materials design for rechargeable metal-air batteries, *Matter* 1 (2019) 565–595, <https://doi.org/10.1016/j.matt.2019.05.008>.
- [3] M. Wu, G. Zhang, M. Wu, J. Prakash, S. Sun, Rational design of multifunctional air electrodes for rechargeable Zn–air batteries: recent progress and future perspectives, *Energy Storage Mater.* 21 (2019) 253–286, <https://doi.org/10.1016/j.ensm.2019.05.018>.
- [4] Y. Chen, S. Ji, S. Zhao, W. Chen, J. Dong, W.C. Cheong, R. Shen, X. Wen, L. Zheng, A.I. Rykov, S. Cai, H. Tang, Z. Zhuang, C. Chen, Q. Peng, D. Wang, Y. Li, Enhanced oxygen reduction with single-atomic-site iron catalysts for a zinc-air battery and hydrogen-air fuel cell, *Nat. Commun.* 9 (2018) 5422, <https://doi.org/10.1038/s41467-018-07850-2>.
- [5] N. Xu, J.A. Wilson, Y.-D. Wang, T. Su, Y. Wei, J. Qiao, X.-D. Zhou, Y. Zhang, S. Sun, Flexible self-supported bi-metal electrode as a highly stable carbon- and binder-free cathode for large-scale solid-state zinc-air batteries, *Appl. Catal. B-Environ.* 272 (2020), 118953, <https://doi.org/10.1016/j.apcatb.2020.118953>.
- [6] I.C. Man, H.Y. Su, F. Calle-Vallejo, H.A. Hansen, J.I. Martínez, N.G. Inoglu, J. Kitchin, T.F. Jaramillo, J.K. Nørskov, C. Rossmeisl, Universality in oxygen evolution electrocatalysis on oxide surfaces, *ChemCatChem* 3 (2011) 1159–1165, <https://doi.org/10.1002/cctc.201000397>.
- [7] J. Rossmeisl, Z.W. Qu, H. Zhu, G.J. Kroes, J.K. Nørskov, Electrolysis of water on oxide surfaces, *J. Electroanal. Chem.* 607 (2007) 83–89, <https://doi.org/10.1016/j.jelechem.2006.11.008>.
- [8] J.R.J.K. Nørskov, A. Logadottir, L. Lindqvist, Origin of the overpotential for oxygen reduction at a fuel-cell cathode, *J. Phys. Chem. B* 108 (2004) 17886–17892.
- [9] C.X. Zhao, J.N. Liu, J. Wang, D. Ren, B.Q. Li, Q. Zhang, Recent advances of noble-metal-free bifunctional oxygen reduction and evolution electrocatalysts, *Chem. Soc. Rev.* 50 (2021) 7745–7778, <https://doi.org/10.1039/d1cs00135c>.
- [10] A.I. Douka, Y. Xu, H. Yang, S. Zaman, Y. Yan, H. Liu, M.A. Salam, B.Y. Xia, A. Zeolitic-Imidazole, Frameworks-derived interconnected macroporous carbon matrix for efficient oxygen electrocatalysis in rechargeable zinc-air batteries, *Adv. Mater.* 32 (2020), 2002170, <https://doi.org/10.1002/adma.202002170>.
- [11] P. Yu, L. Wang, F. Sun, Y. Xie, X. Liu, J. Ma, X. Wang, C. Tian, J. Li, H. Fu, Co nanoclusters rooted on Co-N-C nanosheets as efficient oxygen electrocatalyst for Zn-air batteries, *Adv. Mater.* 31 (2019), 1901666, <https://doi.org/10.1002/adma.201901666>.
- [12] Y. Pan, C. Zhang, Z. Liu, C. Chen, Y. Li, Structural regulation with atomic-level precision: from single-atomic site to diatomic and atomic interface, *Catal., Matter* 2 (2020) 78–110, <https://doi.org/10.1016/j.matt.2019.11.014>.
- [13] X. Wan, X. Liu, Y. Li, R. Yu, L. Zheng, W. Yan, H. Wang, M. Xu, J. Shui, Fe–N–C electrocatalyst with dense active sites and efficient mass transport for high-performance proton exchange membrane fuel cells, *Nat. Catal.* 2 (2019) 259–268, <https://doi.org/10.1038/s41929-019-0237-3>.
- [14] J. Wang, H. Li, S. Liu, Y. Hu, J. Zhang, M. Xia, Y. Hou, J. Tse, J. Zhang, Y. Zhao, Turning on Zn 4s electrons in a N2 -Zn-B2 configuration to stimulate remarkable ORR performance, *Angew. Chem. Int. Ed. Engl.* 60 (2021) 181–185, <https://doi.org/10.1002/anie.202009991>.
- [15] H. Zhou, T. Liu, X. Zhao, Y. Zhao, H. Lv, S. Fang, X. Wang, F. Zhou, Q. Xu, J. Xu, C. Xiong, Z. Xue, K. Wang, W.C. Cheong, W. Xi, L. Gu, T. Yao, S. Wei, X. Hong, J. Luo, Y. Li, Y. Wu, A supported nickel catalyst stabilized by a surface digging effect for efficient methane oxidation, *Angew. Chem. Int. Ed. Engl.* 58 (2019) 18388–18393, <https://doi.org/10.1002/anie.201912785>.
- [16] M. Liu, L. Wang, K. Zhao, S. Shi, Q. Shao, L. Zhang, X. Sun, Y. Zhao, J. Zhang, Atomically dispersed metal catalysts for the oxygen reduction reaction: synthesis, characterization, reaction mechanisms and electrochemical energy applications, *Energy Environ. Sci.* 12 (2019) 2890–2923, <https://doi.org/10.1039/c9ee01722d>.
- [17] J.K. Nørskov, F. Abild-Pedersen, F. Studt, T. Bligaard, Density functional theory in surface chemistry and catalysis, *PNAS* 108 (2011) 937–943, <https://doi.org/10.1073/pnas.1006652108>.
- [18] G.L. Chai, Z. Hou, D.J. Shu, T. Ikeda, K. Terakura, Active sites and mechanisms for oxygen reduction reaction on nitrogen-doped carbon alloy catalysts: Stone-Wales defect and curvature effect, *J. Am. Chem. Soc.* 136 (2014) 13629–13640, <https://doi.org/10.1021/ja502646c>.
- [19] H. Lei, Z.L. Wang, F. Yang, X.Q. Huang, J.H. Liu, Y.Y. Liang, J.P. Xie, M.S. Javed, X. H. Lu, S.Z. Tan, W.J. Mai, NiFe nanoparticles embedded N-doped carbon nanotubes as high-efficient electrocatalysts for wearable solid-state Zn-air batteries, *ARTN* 104293, *Nano Energy* 68 (2020), 104293, <https://doi.org/10.1016/j.nanoen.2019.104293>.
- [20] D. Xie, D. Yu, Y. Hao, S. Han, G. Li, X. Wu, F. Hu, L. Li, H.Y. Chen, Y.F. Liao, S. Peng, Dual-active sites engineering of N-doped hollow carbon nanocubes confining bimetal alloys as bifunctional oxygen electrocatalysts for flexible metal-air batteries, *Small* 17 (2021), 2007239, <https://doi.org/10.1002/smll.202007239>.
- [21] X. Hao, Z. Jiang, B. Zhang, X. Tian, C. Song, L. Wang, T. Maiyalagan, X. Hao, Z. J. Jiang, N-doped carbon nanotubes derived from graphene oxide with embedment of FeCo nanoparticles as bifunctional air electrode for rechargeable liquid and

- flexible all-solid-state zinc-air batteries, *Adv. Sci.* 8 (2021), 2004572, <https://doi.org/10.1002/adv.202004572>.
- [22] L. Zhang, J. Fischer, Y. Jia, X. Yan, W. Xu, X. Wang, J. Chen, D. Yang, H. Liu, L. Zhuang, M. Hankel, D.J. Searles, K. Huang, S. Feng, C.L. Brown, X. Yao, Coordination of atomic Co-Pt coupling species at carbon defects as active sites for oxygen reduction reaction, *J. Am. Chem. Soc.* 140 (2018) 10757–10763, <https://doi.org/10.1021/jacs.8b04647>.
- [23] C.-Y. Su, H. Cheng, W. Li, Z.-Q. Liu, N. Li, Z. Hou, F.-Q. Bai, H.-X. Zhang, T.-Y. Ma, Atomic modulation of FeCo–nitrogen–carbon bifunctional oxygen electrodes for rechargeable and flexible all-solid-state zinc–air battery, *Adv. Energy Mater.* 7 (2017), 1602420, <https://doi.org/10.1002/aenm.201602420>.
- [24] D. Chen, J.W. Zhu, X.Q. Mu, R.L. Cheng, W.Q. Li, S.L. Liu, Z.H. Pu, C. Lin, S.C. Mu, Nitrogen-Doped carbon coupled FeNi₃ intermetallic compound as advanced bifunctional electrocatalyst for OER, ORR and Zn-air batteries, *ARTN 118729*, *Appl. Catal. B-Environ.* 268 (2020), 118729, <https://doi.org/10.1016/j.apcatb.2020.118729>.
- [25] F. Calle-Vallejo, J.I. Martinez, J. Rossmeisl, Density functional studies of functionalized graphitic materials with late transition metals for Oxygen Reduction Reactions, *Phys. Chem. Chem. Phys.* 13 (2011) 15639–15643, <https://doi.org/10.1039/c1cp21228a>.
- [26] Y. Tan, Z. Zhang, Z. Lei, W. Wu, W. Zhu, N. Cheng, S. Mu, Thiourea-Zeolitic imidazolate Framework-67 assembly derived Co–CoO nanoparticles encapsulated in N, S Codoped open carbon shell as bifunctional oxygen electrocatalyst for rechargeable flexible solid Zn–air batteries, *J. Power Sources* 473 (2020), 228570, <https://doi.org/10.1016/j.jpowsour.2020.228570>.
- [27] C. Liu, X. Huang, J. Wang, H. Song, Y. Yang, Y. Liu, J. Li, L. Wang, C. Yu, Hollow mesoporous carbon nanocubes: rigid-interface-induced outward contraction of metal-organic frameworks, *Adv. Funct. Mater.* 28 (2017), 1705253, <https://doi.org/10.1002/adfm.201705253>.
- [28] Z.X. Cai, Z.L. Wang, J. Kim, Y. Yamauchi, Hollow functional materials derived from metal-organic frameworks: synthetic strategies, conversion mechanisms, and electrochemical applications, *Adv. Mater.* 31 (2019), 1804903, <https://doi.org/10.1002/adma.201804903>.
- [29] J. Meng, C. Niu, L. Xu, J. Li, X. Liu, X. Wang, Y. Wu, X. Xu, W. Chen, Q. Li, Z. Zhu, D. Zhao, L. Mai, General oriented formation of carbon nanotubes from metal-organic frameworks, *J. Am. Chem. Soc.* 139 (2017) 8212–8221, <https://doi.org/10.1021/jacs.7b01942>.
- [30] Q. Zhou, S. Hou, Y. Cheng, R. Sun, W. Shen, R. Tian, J. Yang, H. Pang, L. Xu, K. Huang, Y. Tang, Interfacial engineering Co and MnO within N,S co-doped carbon hierarchical branched superstructures toward high-efficiency electrocatalytic oxygen reduction for robust Zn-air batteries, *Appl. Catal. B-Environ.* 295 (2021), <https://doi.org/10.1016/j.apcatb.2021.120281>.
- [31] M. Jiang, J. Yang, J. Ju, W. Zhang, L. He, J. Zhang, C. Fu, B. Sun, Space-confined synthesis of CoNi nanoalloy in N-doped porous carbon frameworks as efficient oxygen reduction catalyst for neutral and alkaline aluminum-air batteries, *Energy Storage Mater.* 27 (2020) 96–108, <https://doi.org/10.1016/j.ensm.2020.01.016>.
- [32] W.J. Wan, X.J. Liu, H.Y. Li, X.Y. Peng, D.S. Xi, J. Luo, 3D carbon framework-supported CoNi nanoparticles as bifunctional oxygen electrocatalyst for rechargeable Zn-air batteries, *Appl. Catal. B-Environ.* 240 (2019) 193–200, <https://doi.org/10.1016/j.apcatb.2018.08.081>.
- [33] Y. Fu, H.-Y. Yu, C. Jiang, T.-H. Zhang, R. Zhan, X. Li, J.-F. Li, J.-H. Tian, R. Yang, NiCo alloy nanoparticles decorated on N-doped carbon nanofibers as highly active and durable oxygen electrocatalyst, *Adv. Funct. Mater.* 28 (2018), 1705094, <https://doi.org/10.1002/adfm.201705094>.
- [34] X. Yan, Y. Jia, X. Yao, Defective structures in metal compounds for energy-related electrocatalysis, *Small Struct.* 2 (2020), 2000067, <https://doi.org/10.1002/sstr.202000067>.
- [35] D. Yang, L. Zhang, X. Yan, X. Yao, Recent progress in oxygen electrocatalysts for zinc-air batteries, *Small Methods* 1 (2017), 1700209, <https://doi.org/10.1002/smt.201700209>.
- [36] S. Li, C. Cheng, X. Zhao, J. Schmidt, A. Thomas, Active salt/silica-templated 2D mesoporous FeCo-Nx-carbon as bifunctional oxygen electrodes for zinc-air batteries, *Angew. Chem. Int. Ed. Engl.* 57 (2018) 1856–1862, <https://doi.org/10.1002/anie.201710852>.
- [37] Q. Lu, J. Yu, X. Zou, K. Liao, P. Tan, W. Zhou, M. Ni, Z. Shao, Self-catalyzed growth of Co, N-codoped CNTs on carbon-encased CoSx surface: a noble-metal-free bifunctional oxygen electrocatalyst for flexible solid Zn–air batteries, *Adv. Funct. Mater.* 29 (2019), 1904481, <https://doi.org/10.1002/adfm.201904481>.
- [38] C. Tang, B. Wang, H.F. Wang, Q. Zhang, Defect engineering toward atomic Co-Nx-C in hierarchical graphene for rechargeable flexible solid Zn-air batteries, *Adv. Mater.* 29 (2017), 1703185, <https://doi.org/10.1002/adma.201703185>.
- [39] G. Jia, W. Zhang, G. Fan, Z. Li, D. Fu, W. Hao, C. Yuan, Z. Zou, Three-dimensional hierarchical architectures derived from surface-mounted metal-organic framework membranes for enhanced electrocatalysis, *Angew. Chem. Int. Ed. Engl.* 56 (2017) 13781–13785, <https://doi.org/10.1002/anie.201708385>.
- [40] Z. Wang, J. Ang, B. Zhang, Y. Zhang, X.Y.D. Ma, T. Yan, J. Liu, B. Che, Y. Huang, X. Lu, FeCo/FeCoNi/N-doped carbon nanotubes grafted polyhedron-derived hybrid fibers as bifunctional oxygen electrocatalysts for durable rechargeable zinc–air battery, *Appl. Catal. B-Environ.* 254 (2019) 26–36, <https://doi.org/10.1016/j.apcatb.2019.04.027>.
- [41] Q. Yang, Y. Jia, F. Wei, L. Zhuang, D. Yang, J. Liu, X. Wang, S. Lin, P. Yuan, X. Yao, Understanding the activity of Co-N_{4-x} C_x in atomic metal catalysts for oxygen reduction catalysis, *Angew. Chem. Int. Ed. Engl.* 59 (2020) 6122–6127, <https://doi.org/10.1002/anie.202000324>.
- [42] C.C. Hou, L. Zou, Q. Xu, A. Hydrangea-Like, Superstructure of open carbon cages with hierarchical porosity and highly active metal sites, *Adv. Mater.* 31 (2019), 1904689, <https://doi.org/10.1002/adma.201904689>.
- [43] Q. Zhang, X.L. Li, B.X. Tao, X.H. Wang, Y.H. Deng, X.Y. Gu, L.J. Li, W. Xiao, N.B. Li, H.Q. Luo, CoNi based alloy/oxides@N-doped carbon core-shell dendrites as complementary water splitting electrocatalysts with significantly enhanced catalytic efficiency, *Appl. Catal. B-Environ.* 254 (2019) 634–646, <https://doi.org/10.1016/j.apcatb.2019.05.035>.
- [44] T. Li, S. Li, Q. Liu, J. Yin, D. Sun, M. Zhang, L. Xu, Y. Tang, Y. Zhang, Immobilization of Ni₃Co nanoparticles into N-doped carbon nanotube/nanofiber integrated hierarchically branched architectures toward efficient overall water splitting, *Adv. Sci.* 7 (2020), 1902371, <https://doi.org/10.1002/adv.201902371>.
- [45] L. Yan, Z.Y. Xu, W.K. Hu, J.Q. Ning, Y.J. Zhong, Y. Hu, Formation of sandwiched leaf-like CNTs-Co/ZnCo₂O₄@NC-CNTs nanohybrids for high-power-density rechargeable Zn-air batteries, *ARTN 105710*, *Nano Energy* 82 (2021), 105710, <https://doi.org/10.1016/j.nanoen.2020.105710>.
- [46] Z. Pei, Y. Huang, Z. Tang, L. Ma, Z. Liu, Q. Xue, Z. Wang, H. Li, Y. Chen, C. Zhi, Enabling highly efficient, flexible and rechargeable quasi-solid-state Zn-air batteries via catalyst engineering and electrolyte functionalization, *Energy Storage Mater.* 20 (2019) 234–242, <https://doi.org/10.1016/j.ensm.2018.11.010>.
- [47] Q. Lu, X. Zou, C. Wang, K. Liao, P. Tan, R. Ran, W. Zhou, M. Ni, Z. Shao, Tailoring charge and mass transport in cation/anion-codoped Ni₃N / N-doped CNT integrated electrode toward rapid oxygen evolution for fast-charging zinc-air batteries, *Energy Storage Mater.* 39 (2021) 11–20, <https://doi.org/10.1016/j.ensm.2021.04.013>.
- [48] Y. Jiang, Y.P. Deng, R. Liang, J. Fu, D. Luo, G. Liu, J. Li, Z. Zhang, Y. Hu, Z. Chen, Multidimensional ordered bifunctional air electrode enables flash reactants shuttling for high-energy flexible Zn-air batteries, *Adv. Energy Mater.* 9 (2019), <https://doi.org/10.1002/aenm.201900911>.
- [49] X.F. Lu, Y. Chen, S. Wang, S. Gao, X.W.D. Lou, Interfacing manganese oxide and cobalt in porous graphitic carbon polyhedrons boosts oxygen electrocatalysis for Zn-air batteries, *Adv. Mater.* 31 (2019), 1902339, <https://doi.org/10.1002/adma.201902339>.
- [50] Y. Tan, W. Zhu, Z. Zhang, W. Wu, R. Chen, S. Mu, H. Lv, N. Cheng, Electronic tuning of confined sub-nanometer cobalt oxide clusters boosting oxygen catalysis and rechargeable Zn–air batteries, *Nano Energy* 83 (2021), 105813, <https://doi.org/10.1016/j.nanoen.2021.105813>.
- [51] X. Liu, L. Wang, P. Yu, C. Tian, F. Sun, J. Ma, W. Li, H. Fu, A stable bifunctional catalyst for rechargeable zinc-air batteries: iron-cobalt nanoparticles embedded in a nitrogen-doped 3D carbon matrix, *Angew. Chem. Int. Ed. Engl.* 57 (2018) 16166–16170, <https://doi.org/10.1002/anie.201809009>.
- [52] D. Deng, L. Yu, X. Chen, G. Wang, L. Jin, X. Pan, J. Deng, G. Sun, X. Bao, Iron encapsulated within pod-like carbon nanotubes for oxygen reduction reaction, *Angew. Chem. Int. Ed. Engl.* 52 (2013) 371–375, <https://doi.org/10.1002/anie.201204958>.
- [53] J. Zhang, Y. Zhao, C. Chen, Y.C. Huang, C.L. Dong, C.J. Chen, R.S. Liu, C. Wang, K. Yan, Y. Li, G. Wang, Tuning the coordination environment in single-atom catalysts to achieve highly efficient oxygen reduction reactions, *J. Am. Chem. Soc.* 141 (2019) 20118–20126, <https://doi.org/10.1021/jacs.9b09352>.
- [54] Z. Chen, Y. Song, J. Cai, X. Zheng, D. Han, Y. Wu, Y. Sang, S. Niu, Y. Liu, J. Zhu, X. Liu, G. Wang, Tailoring the d-band centers enables Co₄N nanosheets to be highly active for hydrogen evolution catalysis, *Angew. Chem. Int. Ed. Engl.* 57 (2018) 5076–5080, <https://doi.org/10.1002/anie.201801834>.
- [55] S.F. Hung, Y.T. Chan, C.C. Chang, M.K. Tsai, Y.F. Liao, N. Hiraoka, C.S. Hsu, H. M. Chen, Identification of stabilizing high-valent active sites by operando high-energy resolution fluorescence-detected X-ray absorption spectroscopy for high-efficiency water oxidation, *J. Am. Chem. Soc.* 140 (2018) 17263–17270, <https://doi.org/10.1021/jacs.8b10722>.
- [56] H. Zhang, W. Zhou, J. Dong, X.F. Lu, X.W. Lou, Intramolecular electronic coupling in porous iron cobalt (oxy)phosphide nanoboxes enhances the electrocatalytic activity for oxygen evolution, *Energy Environ. Sci.* 12 (2019) 3348–3355, <https://doi.org/10.1039/c9ee02787d>.
- [57] Y. Zhu, T.-R. Kuo, Y.-H. Li, M.-Y. Qi, G. Chen, J. Wang, Y.-J. Xu, H.M. Chen, Emerging dynamic structure of electrocatalysts unveiled by in situ X-ray diffraction/absorption spectroscopy, *Energy Environ. Sci.* 14 (2021) 1928–1958, <https://doi.org/10.1039/d0ee03903a>.
- [58] Y. Zhu, H.-C. Chen, C.-S. Hsu, T.-S. Lin, C.-J. Chang, S.-C. Chang, L.-D. Tsai, H. M. Chen, Operando unraveling of the structural and chemical stability of P-substituted CoSe₂ electrocatalysts toward hydrogen and oxygen evolution reactions in alkaline electrolyte, *ACS Energy Lett.* 4 (2019) 987–994, <https://doi.org/10.1021/acsenenergylett.9b00382>.
- [59] H. Zhang, W. Zhou, X.F. Lu, T. Chen, X.W. Lou, Implanting isolated Ru atoms into edge-rich carbon matrix for efficient electrocatalytic hydrogen evolution, *Adv. Energy Mater.* 10 (2020), <https://doi.org/10.1002/aenm.202000882>.
- [60] Y. Zhu, J. Wang, H. Chu, Y.-C. Chu, H.M. Chen, In situ/operando studies for designing next-generation electrocatalysts, *ACS Energy Lett.* 5 (2020) 1281–1291, <https://doi.org/10.1021/acsenenergylett.0c00305>.